Vol. 75: 65–80, 2018
https://doi.org/10.3354/cr01507

CLIMATE RESEARCH
Clim Res

Published online April 18

Influence of climate oscillations on urban and rural temperature variability in the Kanto region of Japan

M. X. C. Seow[1,*], M. Roth[2]

[1]Department of Earth and Planetary Science, Graduate School of Science, The University of Tokyo, Tokyo 113-0033, Japan
[2]Department of Geography, National University of Singapore, 117570, Singapore

ABSTRACT: Climate oscillations of air and sea-surface temperatures are known to influence surface temperature and precipitation variability. Intraseasonal (4 to 12 mo) and interannual (>12 to 120 mo) variability is investigated using monthly mean temperature data from 4 urban and 3 rural weather stations located in the Kanto region of Japan, during the period January 1973–August 2015. Indices of 6 climate oscillations (El Niño–Southern Oscillation, Indian Ocean Dipole, Quasi-Biennial Oscillation, Arctic Oscillation, Pacific North American Pattern and West Pacific Pattern) known to influence Japan's climate are investigated using wavelet analysis to identify oscillations in temperature data and climate mode indices at various periods. The continuous wavelet transform analysis shows that temperature variability is more pronounced at the intraseasonal than interannual timescale and urbanisation has no influence on temperature variability. Using the wavelet transform coherence analysis, all climate oscillations except El Niño–Southern Oscillation significantly covary with the temperature at certain periods and years, with the West Pacific Pattern having the highest coherence on average across the whole study period and analysed timescales. On average across the study period, using the multiple linear regression technique, only the Arctic Oscillation and West Pacific Pattern are found to significantly contribute to both intraseasonal and interannual temperature variability.

KEY WORDS: Climate variability · Air temperature · Urban–rural stations · Wavelet analysis · Japan's climate

1. INTRODUCTION

Climatic changes, with respect to temperature, experienced across the world, particularly over the last century, are influenced by human and natural factors. Long-term temperature change, known as global warming, is attributed to increasing atmospheric greenhouse gas concentrations due to anthropogenic activity. Increasing urbanisation over time also contributes to stronger warming trends experienced in cities (Oke, 1982, Fujibe 2009, Santamouris 2015). Another type of change is temperature variability, which refers to temperature fluctuations about a mean. It is caused by naturally occurring climate oscillations at various timescales.

Apart from global warming, temperature variability can bring social and economic problems. Temperature variability is an emerging issue for highly populated areas such as the Kanto region (KR) in Japan, which was home to 42 million people in 2010, corresponding to a third of Japan's population. Climate oscillations, coupled with global warming, are associated with health issues, including disease transmission and heat-related illnesses. In Japan, death tolls from heatstroke and cases of infectious diseases are found to be strongly linked to temperature variability brought by the El Niño–Southern Oscillation (ENSO) and Indian Ocean Dipole (IOD) (Zaraket et al. 2008, Akihiko et al. 2014). A better understanding of the roles of climate oscillations on temperature variabil-

*Corresponding author: xcmarvin@eps.s.u-tokyo.ac.jp

ity is critical for producing better climate forecasts and implementing early health warning systems serving the large urban and rural populations of KR.

In the context of Japan, numerous climate studies have focused on the long-term warming trend between urban and rural areas. Several studies (e.g. Fujibe 2009, Kataoka et al. 2009, Yamato et al. 2011) have concluded that the urban areas tend to be warmer than nearby rural areas and the urban heat island intensities are increasing with time. This observation is consistent with those in other parts of Asia (Kataoka et al. 2009).

Currently there is no comprehensive study considering the relationship between Japan's temperature and multiple climate oscillations at decadal to centurial time scales, as well as urban–rural differences. Prokoph & Patterson (2004) is the only comparative study of urban–rural temperature variability, comparing monthly mean urban and rural temperature variability in western Ontario. These authors found that urban and rural areas exhibit temperature fluctuations of similar frequencies and magnitudes at common time periods, thereby showing that urbanisation does not affect long-term temperature variability. The authors postulated that any variability in urban and rural temperatures at interannual and interdecadal timescales is related to natural oscillations, although they did not investigate this further using climate oscillation indices.

Six climate oscillations with dominant intraseasonal (4 to 12 mo) and/or interannual (>12 to 120 mo) components are known to influence Japan's climate. They are ENSO, IOD, the Quasi-Biennial Oscillation (QBO), the Arctic Oscillation (AO), the Pacific North American Pattern (PNAP) and the West Pacific Pattern (WPP). The first 3 are tropical phenomena and the latter 3 are mid-latitude or polar phenomena. ENSO, the global leading mode of interannual and interdecadal sea-surface temperature (SST) variability, is found to bring a cooler autumn, and a warmer spring and winter to KR during El Niño, although no significant temperature anomalies are seen during La Niña (Bridgman & Oliver 2014, Japan Meteorological Agency 2015a,b). IOD, the second leading internal mode of interannual SST variability, which is unique to the Indian Ocean, has been confirmed to bring a warmer (cooler) summer to Japan during its positive (negative) phase (Japan Agency for Marine–Earth Science and Technology 2003, Saji & Yamagata 2003). QBO, characterised by the reversal of lower stratospheric zonal winds from west to east every 2 to 3 yr, is known to reduce (increase) spring rainfall over Japan during its westerly (easterly) phase (Seo et al. 2013, Bridgman & Oliver 2014), although its impact on temperature has yet to be evaluated. AO, characterised by the fluctuation of low-tropospheric pressures between the northern polar and mid-latitude regions from the interannual to millennial timescales, is observed to trigger more (fewer) cold surges and a colder (warmer) winter in Japan during its negative (positive) phase (Park et al. 2010, 2011, Darby et al. 2012). PNAP, which describes the intraseasonal and interannual fluctuations of mid-tropospheric pressures between western and eastern North America, is found to cause a colder (warmer) winter in Japan during its positive (negative) phase (Yang et al. 2002, Bridgman & Oliver 2014). Finally, WPP, which describes the intraseasonal and interannual fluctuations of mid-tropospheric pressures in eastern Siberia and the western North Pacific, is known to cause positive (negative) temperature anomalies in Japan during winter (Oshika et al. 2015, Park & Ahn 2016).

The aims and organisation of this paper are as follows. A brief description of the data and methodology used is given in the next section. Focusing on the period January 1973–August 2015, this paper investigates the leading modes of temperature variability and compares urban–rural temperature variability across the KR in Section 3.1. Section 3.2 covers the long-term covarying relationships that the temperature has with various climate modes and the individual contribution of each climate mode to temperature variability. Since the data are only ~40 yr long and monthly averages are used, climate oscillations without any intraseasonal or interannual components, like the Pacific Decadal Oscillation, are excluded from this study.

2. STUDY AREA, DATA AND METHODS

2.1. Study area and stations

The KR consists of the central part of Honshu Island, Japan. It includes Greater Tokyo, one of the most populous metropolitan areas in the world (Fig. 1a). Its total area is 32 000 km^2, with the lowland area (herein defined as <150 m above sea level) occupying ~17 000 km^2 or half of KR. Mountains to the north and west of KR form the Central Highlands. KR experiences a humid subtropical climate (Köppen climate classification Cfa) dominated by the annual East Asian monsoon (Kurita et al. 2015). According to the Japan Meteorological Agency (2017), during winter (December–February), winter monsoonal

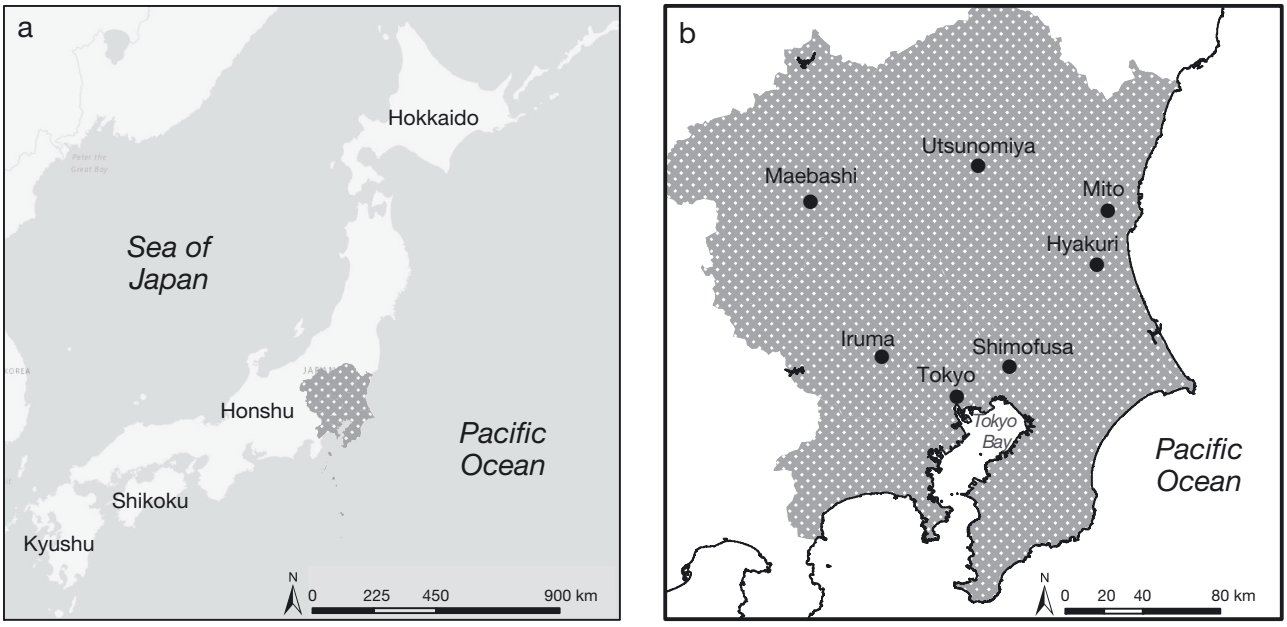

Fig. 1. (a) Location of the study area, the Kanto region (hatched) in Japan. (b) Locations of 7 meteorological stations that provided data for the study of urban and rural temperature variability

northwesterlies bring cold, dry Siberian air to KR. During spring (March–May), migratory anticyclones and cyclones result in temperature swings and alternating dry and wet periods. During summer (June–August), warm, moist summer monsoonal southwesterlies results in the Baiu front bringing cloudy, wet weather. From mid-July to August, the North Pacific High brings hot, sunny weather to KR, while during autumn (September–November), the active autumnal front and tropical cyclones may result in heavy precipitation, making this the wettest season. However, the weather turns sunny and cooler in October and November with frequent passages of anticyclones.

A total of 7 meteorological stations across KR were selected for this study, using 4 criteria. (1) The daily mean temperature data are sufficiently complete such that monthly mean temperatures can be calculated for >99% of the study period (at least 512 out of 516 months). This is to fulfil a condition of wavelet analysis that requires uninterrupted data. To maintain an uninterrupted time series, missing monthly mean data are replaced by zeros. (2) Elevations of selected stations are <150 m, in line with this paper's focus on lowland stations. (3) Stations are sited in distinct urban and rural areas, where the land use/land cover (LULC) type within 0.5 km of the station is generally homogeneous, to allow classification as either urban or rural. Fourth, following Sakakibara & Owa (2005), only stations located inland are selected, to enable assessment of the urban effect. This is because marine air advection can influence coastal temperatures and cause climatic variations between inland and coastal areas. Moreover, all stations selected are within 200 km of each other, so that synoptic climate variations between them are likely to be small, again in order to be able to evaluate urban–rural temperature variability differences. Tokyo station was moved to a new location (0.9 km away from its previous location) on 2 December 2014 (Japan Meteorological Agency 2016). Thus, a slight discontinuity in the temperature time series is to be expected. Despite this change, the new station's surrounding environment is still dominantly urban; moreover only 9 out of 516 months (~2%) of temperature data used for this study was recorded at the new station location, which would have little effect on the wavelet analysis results, particularly for the interannual frequency band. The station locations are shown in Fig. 1b, and station characteristics are summarised in Table 1.

To further ascertain that synoptic temperature variations among stations are small, seasonal mean temperatures for each station based on the period January 1973–August 2015 are tabulated in Table 2. Of all seasons, the temperature range is the largest during winter (3.7°C); this can be attributed to the pronounced winter urban heat island effect (Sakakibara & Owa 2005). Nonetheless, within each season, the standard deviations and ranges of mean tempera-

Table 1. Geographic coordinates and land use/land cover (LULC) of urban and rural meteorological stations in Kanto, Japan, in 1976, 1997 and 2014. The Tokyo station was relocated in November 2014; data in parentheses are for the new location, from December 2014 onwards. Letter codes show the dominant LULC; in mixed LULC areas, the subscript letter code indicates the second-ranked LULC. G: open field or bare soil; T: trees such as orchard or forest; U: urbanised area

Station	Latitude (°N)	Longitude (°E)	Elevation (m)	LULC 1976	LULC 1997	LULC 2014
Urban						
Maebashi	36.400	139.066	114	U	U	U
Mito	36.381	140.468	76	U	U	U
Tokyo	35.683	139.766	36	U	U	U
	(35.692)	(139.751)	(24)			(U_T)
Utsunomiya	36.550	139.866	140	U_T	U	U
Rural						
Hyakuri	36.181	140.415	32	G	G	G
Iruma	35.833	139.417	90	G	G	G_U
Shimofusa	35.798	140.011	30	G_T	G_T	G

Table 2. Seasonal mean temperatures (°C) of urban and rural meteorological stations in Kanto, Japan, for the period January 1973–August 2015

Station	Winter (DJF)	Spring (MAM)	Summer (JJA)	Autumn (SON)
Urban				
Maebashi	4.3	12.8	24.4	16.5
Mito	3.9	11.8	22.9	16.0
Tokyo	6.9	14.3	25.1	18.5
Utsunomiya	3.4	12.2	23.6	16.0
Rural				
Hyakuri	3.2	11.4	22.5	15.5
Iruma	4.3	12.8	24.0	16.4
Shimofusa	5.3	13.3	24.1	17.1

tures amongst all stations are still below 1.3°C and 3.7°C respectively, which implies that temperature variations among all stations are small across all seasons.

The latest LULC type surrounding each station is assessed using satellite images taken in 2014 and hosted on the Esri–DigitalGlobe ArcGIS World Imagery basemap service. To confirm if the LULC type has changed significantly over the study period, past LULC types are determined using LULC pattern-grid maps obtained from the Japan's Ministry of Land, Infrastructure, Transport and Tourism (http://nlftp.mlit.go.jp/ksj-e/index.html). The earliest maps date back to 1976, and they have been produced around once every decade since then. Each grid corresponds to 0.01 km^2, and different grid patterns represent various LULC types. LULC maps for 1976 and 1997 are analysed. Only the area close enough to influence the station temperature, which is within 0.5 km from the station, is assessed (Oke 2006). Past LULC maps identify urban areas without revealing their built types (building density, height and size). Hence, stations are classified into either urban or rural (vegetated, forested) categories based on the dominant LULC type within the 0.5 km radial zone for 1976 and 1997. The dominant LULC type is determined (and, if any, a second-ranked LULC type occupying at least 20% of the area) by calculating and ranking the area percentages for all LULC types with ArcGIS version 10.2.1. The LULC maps and satellite imageries indicate that for all stations, urban areas in 1976 are still predominantly urban in 2014, and the same applies to rural areas. The LULC types for all stations in 1976, 1997 and 2014 are shown in Table 1.

2.2. Data

The data used in this study include temperature time series from 7 stations and the 6 climate oscillation indices mentioned earlier. Daily mean temperature data for the stations from January 1973 to August 2015 are taken from the National Climatic Data Center (https://www.ncdc.noaa.gov/cdo-web/). Monthly mean indices of ENSO, AO, PNAP and WPP for the same time period are retrieved from the NOAA Climate Prediction Center, while those of QBO are taken from the NOAA Earth System Research Laboratory (www.esrl.noaa.gov/psd/data/climateindices/list/). Several indices measuring the ENSO intensity, including the Southern Oscillation Index and Niño SST 3.4 indices, have been established, but this study employs the Multivariate ENSO Index (MEI), which is the most holistic index: it captures the ENSO phenomenon by incorporating 6 variable fields (sea surface pressure, SST, zonal and meridional surface winds, surface temperature and total cloudiness fraction) instead of only 1 variable field as other indices do (Wolter & Timlin 1998). Monthly mean indices for the IOD, represented by the Dipole Mode Index (DMI), from January 1973 to August 2015 are obtained from the Japan Agency for Marine–Earth Science and Technology (www.jamstec.go.jp/frsgc/research/d1/iod/iod/dipole_mode_index.html).

To remove the effect of the seasonal cycle on temperature data, monthly mean temperature data are normalised by calculating monthly means and standard deviations of the base period January 1973–August 2015 to obtain monthly normalised temperature anomalies. Due to missing daily temperature data for some stations, anomalies for months with <16 d of daily values are not calculated but instead replaced with zeros (i.e. the means of monthly anomalies) to maintain an uninterrupted time series. For any given station, not more than 5 months are replaced with zeros. Intraseasonal (4 to 12 mo) and interannual (12 to 120 mo) signals are extracted using a band-pass Butterworth filter, as displayed in Fig. 2.

2.3. Wavelet analysis

The wavelet analysis is employed to identify the leading modes of temperature variability within a temperature time series, as well as to establish any covarying relationship between temperature and a given climate oscillation. The wavelet analysis has been applied in many meteorological studies investigating interdecadal climate oscillations (e.g. Torrence & Webster 1999, Lucero & Rodríguez 2000). It decomposes the time series into the time–frequency space, in contrast to the standard Fourier transform that reveals only the frequency space. The time–frequency space allows easy identification of dominant modes of variability and changes in amplitude of oscillation over various frequencies and times. It is a useful method to identify non-stationarity or quasi-periodicity in meteorological time series (Prokoph & Patterson 2004).

According to Addison (2002), the continuous wavelet transform (CWT) is used to identify the leading modes of temperature variability. By varying the widths of filtering functions called wavelets, the CWT generates a set of wavelet coefficients used to construct the time–frequency representation of a time series. In practice, a continuous time series is standardised for easier detection of fluctuations and discretised into values of x_n at time index n, with 2 consecutive values separated by a constant time interval δt. The wavelet coefficients $W_n(s)$ are calculated from the convolution of the time series with a mother wavelet ψ:

$$W_n(s) = \sum_{k=0}^{N-1} x_n \psi^* \left[\frac{k-n}{s} \right] \delta t \quad (1)$$

where N is the length of time series, * indicates the complex conjugate, k is the wavelet translation parameter controlling the wavelet position along the time axis and s is the wavelet scale or period. Climate signal processing studies often uses the Morlet wavelet because of its better frequency resolution (Baliunas et al. 1997). The Morlet wavelet is the product of a complex sinusoid and Gaussian function:

$$\psi(t) = \pi^{-1/4} e^{i\omega_0 t - t^2/2} \quad (2)$$

where t is the time parameter and ω_0 is the frequency parameter, which is set to 6 for Morlet wavelet to satisfy the wavelet's admissibility condition of having a zero mean (Farge 1992). According to Torrence & Compo (1998), from the definition of power in Fourier analysis, the wavelet power of time series, which indicates the magnitude of oscillation at period s and at given time associated with k, is the squared wavelet coefficient $|W|^2$. The global power $\left|\overline{W_n}(s)\right|^2$ at scale s, which is the averaged wavelet power across the whole length of time series, is:

$$\left|\overline{W_n}(s)\right|^2 = \frac{1}{N} \sum_{k=0}^{N-1} \left|W_n(s)\right|^2 \quad (3)$$

As noted by Liu et al. (2007), the calculated $|W|^2$ based on Fourier's definition tends to overestimate (underestimate) magnitudes of low (high) frequency oscillations, making the comparison of power across different periods difficult. This is because the orthonormal basis of wavelet transform leads to $|W|^2$ being equivalent to the product of true wavelet power and scale s. Thus, bias-rectified spectra are generated using the scaling-correction method developed by Liu et al. (2007), dividing $|W|^2$ by s to obtain the rectified, true power.

The areas near to edges of the power spectrum are where the wavelet power is reduced. These areas are defined as the cone of influence (COI), which are marked out in the spectra and should be interpreted with caution (Addison 2002).

Strong power peaks in the CWT spectra are identified using statistical significance tests by comparing the unrectified $|W|^2$ against a red-noise function. Assuming that W is normally distributed, the normalised $|W|^2$ follows a chi-square (χ^2) distribution with 2 degrees of freedom. In this paper, strong peaks are significant at the 95% confidence level. The critical value at 95% level is determined by the product of 95-percentile value of χ^2 and red-noise spectrum (Gilman et al. 1963). The robustness of significance tests used in CWT spectra is based on the Gaussian red-noise function that assumes normality (Torrence & Compo 1998). Thus, the normality of time series is confirmed using the 1-sample Kolmogorov–Smirnov test at the 95% confidence level.

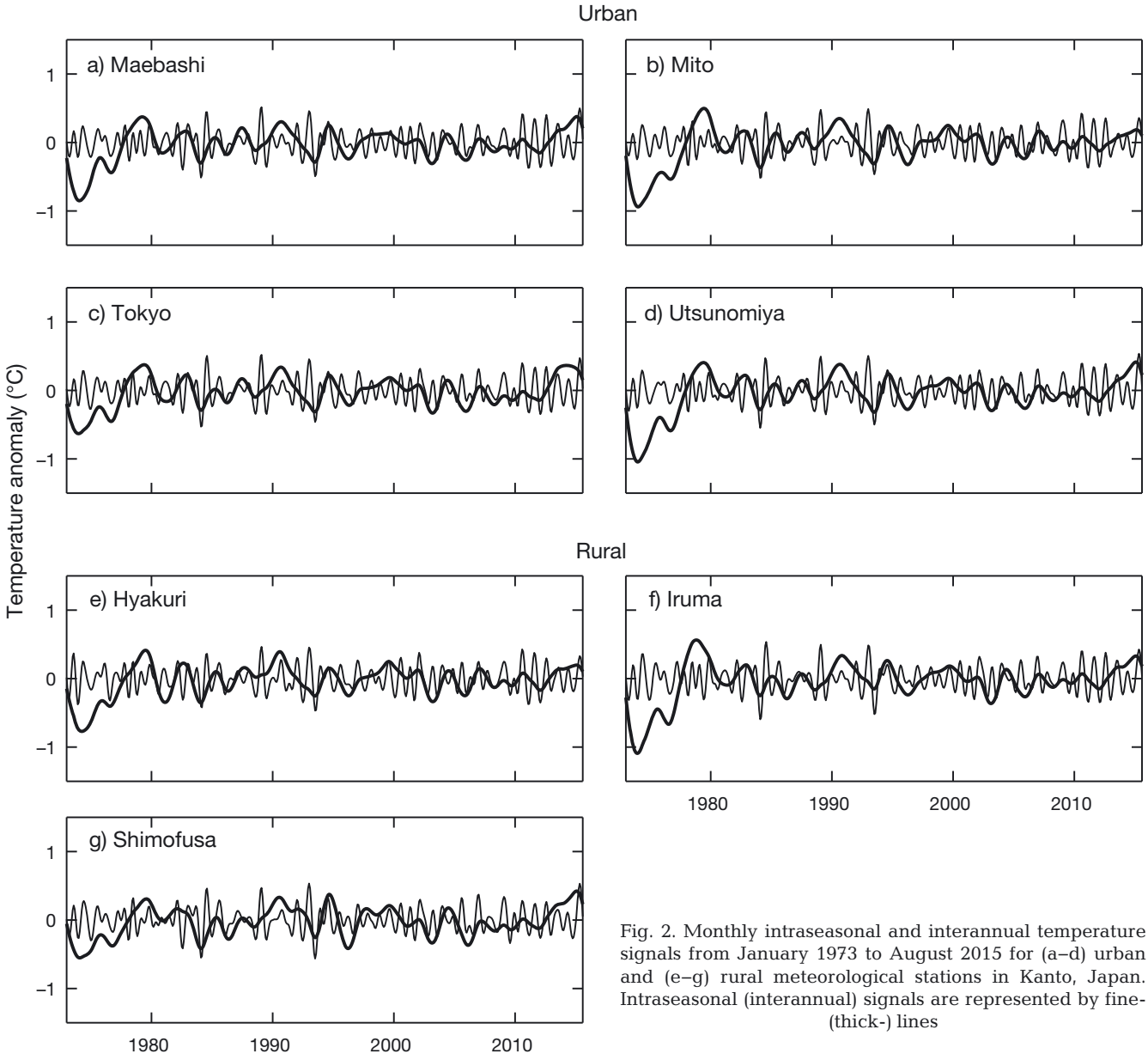

Fig. 2. Monthly intraseasonal and interannual temperature signals from January 1973 to August 2015 for (a–d) urban and (e–g) rural meteorological stations in Kanto, Japan. Intraseasonal (interannual) signals are represented by fine- (thick-) lines

Except for the QBO index, all temperature and climate oscillation index time series are identified to be normally distributed. The QBO index is therefore converted to percentiles and transformed to z-scores using the normal inverse cumulative distribution function. This forces the QBO index to adhere to the standard normal distribution.

To determine how a given temperature time series X and a given climate oscillation index Y at time index n and scale s covary with each other, the wavelet transform coherence (WTC), known as the coefficient of determination for frequency, is calculated. The coherence $R_n^2(s)$ is defined by

$$R_n^2(s) = \frac{\left|S^{XY}\left(s^{-1}W_n^{XY}(s)\right)\right|^2}{S^X\left(s^{-1}\left|W_n^X(s)\right|^2\right)S^Y\left(s^{-1}\left|W_n^Y(s)\right|^2\right)}, \quad (4)$$

where $W_n{}^X$ and $W_n{}^Y$ are the wavelet coefficients of X and Y respectively, $W_n{}^{XY}$ is the cross-wavelet transform of X and Y, and S^X, S^Y and S^{XY} are the smoothing operators. The phase difference of an identified periodicity between X and Y is calculated from the phase difference between the real and imaginary parts of $W_n{}^{XY}$.

Since the coherence is normalised, R^2 ranges from 0 to 1, where 1 indicates the strongest cross-correla-

tion. Also, the COI in the WTC spectrum is marked out using a similar method as for the CWT spectra. According to Grinsted et al. (2004), significantly strong R^2 values can be identified using Monte Carlo methods. Strong R^2 values are significant at the 95% level. Since R^2 values are not known to follow any statistical distribution, the critical values at 95% level are determined empirically. For a given scale *s*, the critical value is estimated by generating 1000 Gaussian white-noise time series and taking data pairs outside of the COI using the Monte Carlo method. R^2 values higher than the critical value are delineated in the WTC spectra.

The CWT spectra are generated using the MATLAB package by Torrence & Compo (1999) that is corrected for bias rectification. The WTC spectra are generated using the MATLAB package by Grinsted (2014).

3. RESULTS AND DISCUSSION

3.1. Urban–rural temperature variability differences

Each CWT spectrum of temperature time series across the entire study period shown in Fig. 3 is accompanied by its respective global power spectrum generated with Eq. (3). The CWT spectrum is represented in time–frequency space, with shaded areas indicating strong wavelet power or periodicity at periods and years covered by the shaded areas. The most notable broad pattern among all CWT spectra is quasi-periodicity, which is present in all temperature time series. Quasi-periodicity is indicated by the presence of dense shaded patches in Fig. 3, instead of large, extensive shaded areas, and occurs especially at the intraseasonal timescale. Also, the varying vertical and horizontal widths and power intensity of shaded patches across the entire time interval reveal that the magnitudes and frequencies of temperature variability are changing. They imply that temperature variability is characterised by a series of alternating active and break periods without fixed lifetimes, another characteristic of quasi-periodicity. A second common pattern is the presence of strongest intraseasonal variability in all CWT spectra at the 4–8 mo period in 1976–1985. A third common pattern is there are 3 common time intervals of peak interannual variability at the 16–64 mo period across all stations. Broadly speaking they occur in 1980–1987, 1990–1998 and 2002–2010.

Among all global power spectra, generally two primary peak powers occur at the 4–12 mo period, and a secondary peak occurs at the ~32 mo period. The CWT and global power spectra suggest that temperature variability is stronger at the intraseasonal than interannual timescale, thereby indicating intraseasonal variability as the primary leading frequency mode.

Sections of global power spectra from the intraseasonal and interannual timescales from different stations are compared to study the difference in temperature variability between 2 given stations using the root mean-square error (RMSE) metric. The results are tabulated for both intraseasonal and interannual timescales in Tables 3 & 4, respectively. At both intraseasonal and interannual timescales, there is no consistent pattern in the RMSEs between urban–urban/rural–rural, and urban–rural stations, where a specific group of RMSEs is consistently higher than the other group. For instance, focusing on RMSEs involving Mito station, the RMSEs between Mito and Maebashi stations (urban–urban) are greater than those between Mito and Hyakuri stations (urban–rural), but those for other urban–urban station differences are lower than those between Mito and Hyakuri stations (Tables 3 & 4). This implies differences between RMSEs are due to inherent local climatic variations between different stations. The same observation applies for the rest of the stations. Futhermore, the 2-sided Wilcoxon rank sum test reveals no significant difference between the 2 groups of RMSEs (urban–urban/rural–rural, and urban–rural differences) at the 95% level for the intraseasonal ($p = 0.19$) or interannual timescale ($p = 0.23$). Hence, there is no conclusive evidence indicating that urbanisation influences temperature variability.

3.2. Relationships between climate oscillations and temperature

To explore the covarying relationship between each climate oscillation and temperature, WTC spectra are generated for all 7 stations for each climate oscillation. For each climate oscillation, the WTC spectra of all stations are expected to not differ significantly from each other. This is because, from Eq. (4), the wavelet coherence is analogous to the normalised squared covariance (or correlation), where the normalisation will not account for magnitudes of variability in the temperature and climate oscillation. Given that all stations are located close together at the synoptic scale, it should follow that a given cli-

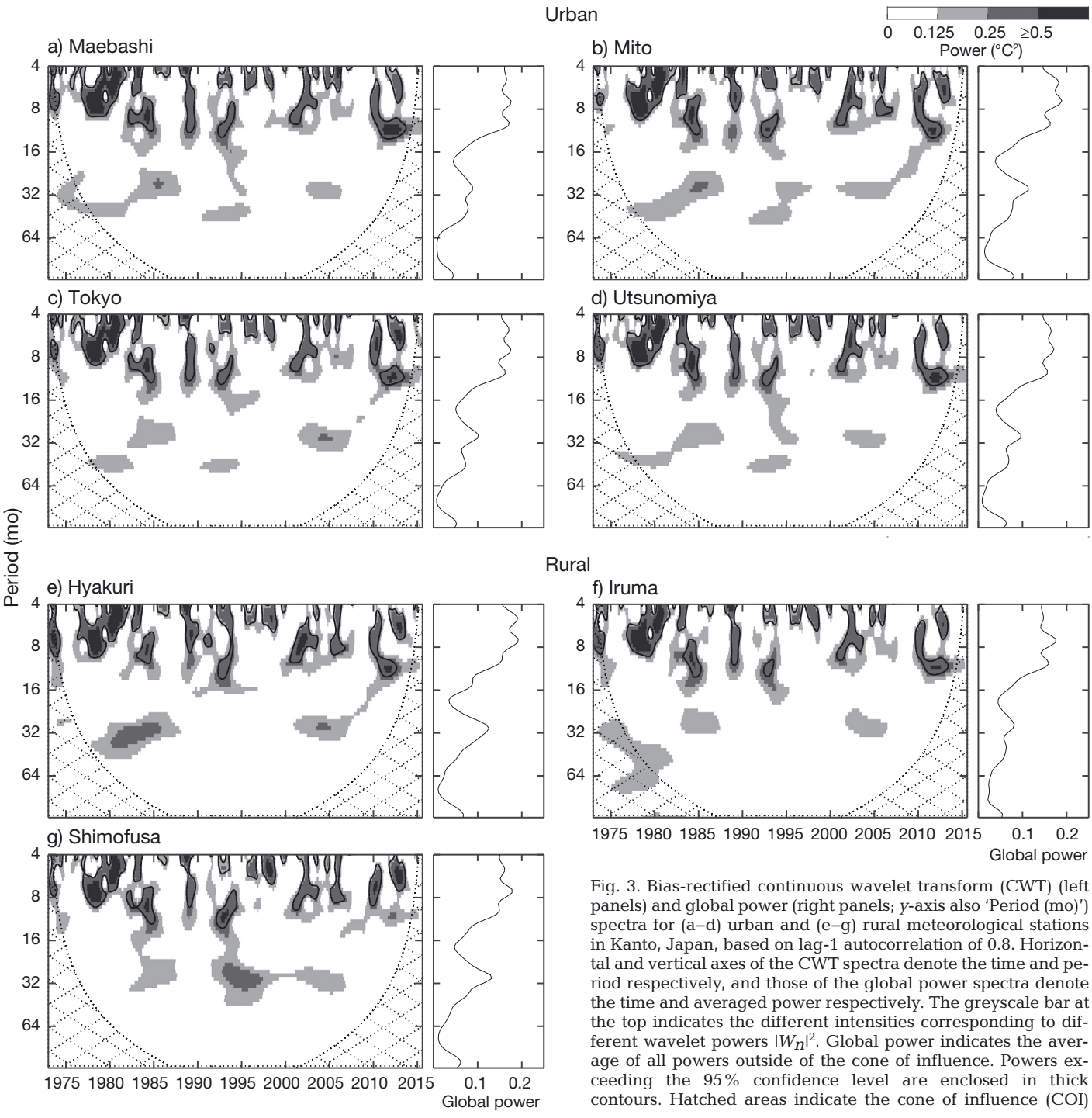

Fig. 3. Bias-rectified continuous wavelet transform (CWT) (left panels) and global power (right panels; *y*-axis also 'Period (mo)') spectra for (a–d) urban and (e–g) rural meteorological stations in Kanto, Japan, based on lag-1 autocorrelation of 0.8. Horizontal and vertical axes of the CWT spectra denote the time and period respectively, and those of the global power spectra denote the time and averaged power respectively. The greyscale bar at the top indicates the different intensities corresponding to different wavelet powers $|W_n|^2$. Global power indicates the average of all powers outside of the cone of influence. Powers exceeding the 95% confidence level are enclosed in thick contours. Hatched areas indicate the cone of influence (COI)

mate oscillation correlates with temperatures of all stations by almost the same extent at broadly similar specific periods and years. The WTC spectra generated for all 7 stations are indeed broadly similar. For this reason, only the WTC spectra for Tokyo are shown in Fig. 4. Tokyo is used as the representative station for KR, as designated by the Japan Meteorological Agency (2017), to analyse the relationships of temperature in KR with the 6 climate oscillations throughout this paper.

In Fig. 4, the WTC spectrum is represented in time–frequency space, with the vertical and horizontal axes denoting the period and time respectively. In each WTC spectrum, shaded areas enclosed in thick contours (exceeding the 95% level) indicate very high coherence ($R^2 > \sim 0.7$), shaded areas without contours in-

Table 3. Matrix of calculated RMSE (× 10^{-2} °C) of global power spectra between pairs of urban and rural meteorological stations in Kanto, Japan at the intraseasonal timescale for the period January 1973–August 2015

	Urban stations			Rural stations		
Station	Maebashi	Mito	Tokyo	Utsunomiya	Hyakuri	Iruma
Urban						
Mito	0.92	–	–	–	–	–
Tokyo	0.45	0.69	–	–	–	–
Utsunomiya	0.69	0.90	0.3	–	–	–
Rural						
Hyakuri	1.31	0.77	1.13	1.33	–	–
Iruma	0.98	1.48	0.95	0.75	1.90	–
Shimofusa	1.03	1.17	0.81	0.61	1.30	0.87

Table 4. Matrix of calculated RMSE (× 10^{-2} °C) of global power spectra between pairs of urban and rural meteorological stations in Kanto, Japan at the interannual timescale for the period January 1973–August 2015

	Urban stations			Rural stations		
Station	Maebashi	Mito	Tokyo	Utsunomiya	Hyakuri	Iruma
Urban						
Mito	1.30	–	–	–	–	–
Tokyo	0.71	1.05	–	–	–	–
Utsunomiya	0.75	0.89	0.64	–	–	–
Rural						
Hyakuri	1.59	0.91	1.49	1.43	–	–
Iruma	1.02	1.49	1.00	0.89	1.92	–
Shimofusa	1.73	1.17	1.50	1.53	1.01	2.05

dicate high coherence ($0.5 < R^2 < \sim 0.7$) and non-shaded areas indicate low coherence ($R^2 < 0.5$) at those periods and times. Phase differences between both time series are indicated (only on shaded areas) with vectors. With degrees indicating rotation in a clockwise direction, vectors pointing up [0°] (down [180°]) indicate both series are in-phase (anti-phase) with each other. Vectors pointing right [90°] and left [270°] indicate that the phases of temperature and climate oscillation index differ by a quarter cycle. Since the coherence is normalised, the WTC spectrum can identify time–frequency regions with high coherence even when wavelet powers of temperature and climate oscillation index time series in such regions are low. It is important to refer to both vectors and shaded areas to conclude if temperature variability and climate oscillation are related to each other. If they are related, there should be evidence of phase-locking. This means that most vectors, especially those on very high coherence areas, at a particular period throughout the entire study period should point consistently in a specific direction. Random vector directions indicate a lack of phase-locking and the random nature of such high coherence, which means that the climate oscillation is unlikely to cause the temperature variability.

In addition to analysing the WTC spectra, the CWT and global power spectra for each climate oscillation index are generated as shown in Fig. 5. The CWT and global power spectra allow us to identify the dominant frequency modes in climate oscillations to assist in the WTC spectrum analysis. For MEI (Fig. 5a), the CWT spectrum shows no visible intraseasonal but strong interannual variability at the 16–64 mo period, particularly during 1975–2002 and 2008–2013 as indicated by the thick contours. For DMI (Fig. 5b), strong intraseasonal variability at periods >8 mo is observed. Its intraseasonal variability peaks in 1981–1984. Such intraseasonal variability tends to be short-lived, lasting for 1 to 3 yr, and is interrupted by longer break time intervals of >5 yr. The interannual IOD variability at the 16–64 mo period peaks in 1985–2000 but tends to be significantly weaker or absent in other years. For the QBO index (Fig. 5c), while intraseasonal variability is negligible, strong, uninterrupted interannual variability at the 28–32 mo period is seen across the whole study period. The AO, PNAP and WPP indices (Fig. 5d–f) display strong intraseasonal variability, interrupted by break periods throughout the whole study period at the 4–8 mo period. The interannual variability is weaker in comparison and occurs sporadically in certain years. For example, active interannual variability at the ~32 mo period for the WPP index is only present in 1980–1990. Comparing between the global spectra in Figs. 3 and 5, the strongest temperature variability at the 4–8 mo period corresponds to the rather strong intraseasonal signals in the AO, PNAP and WPP indices, and the secondary peak variability at the ~32 mo period corresponds to the strong interannual signals in the MEI, DMI and QBO index. The WTC will further illustrate which climate mode(s) are significantly linked to the strong temperature variability at those mentioned periods. Also, generally, some climate oscillations display distinct interdecadal variations in their interannual signals, particularly for ENSO, IOD and WPP, which affect the covarying relationship

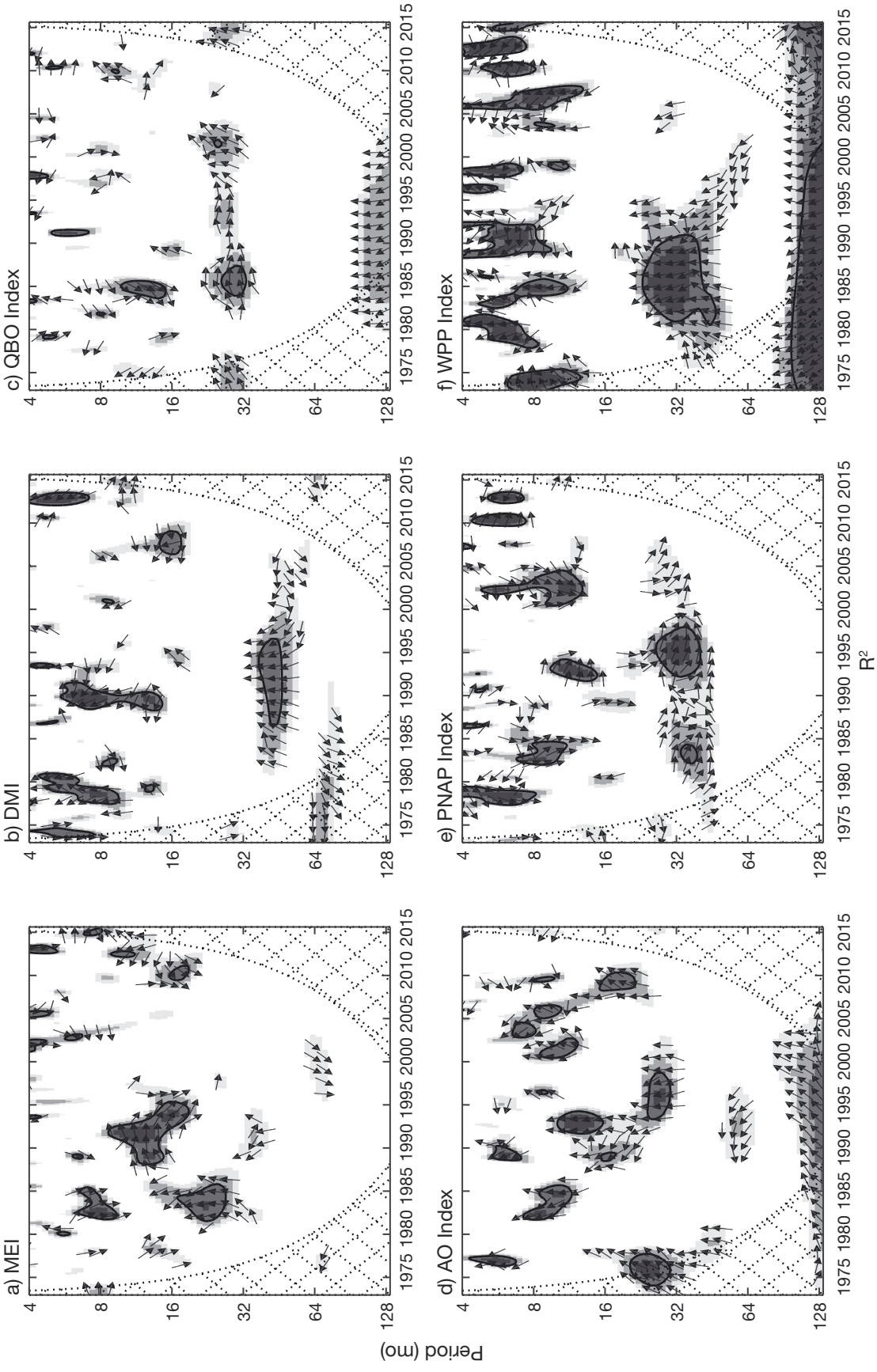

Fig. 4. Wavelet transform coherence spectra showing coherence R^2 values between temperature at the Tokyo meteorological station and 6 indices of climate oscillations (MEI: Multivariate ENSO Index; DMI: Dipole Mode Index; QBO: Quasi-biennial Oscillation; AO: Arctic Oscillation; PNAP: Pacific North American Pattern; WPP: West Pacific Pattern). Vertical and horizontal axes denote the period and time respectively. The greyscale bar at the bottom indicates R^2 values. R^2 values exceeding the 95% confidence level are enclosed in thick contours. Hatched areas indicate the cone of influence (COI). Phase differences represented by vectors are indicated on shaded areas with $R^2 > 0.5$

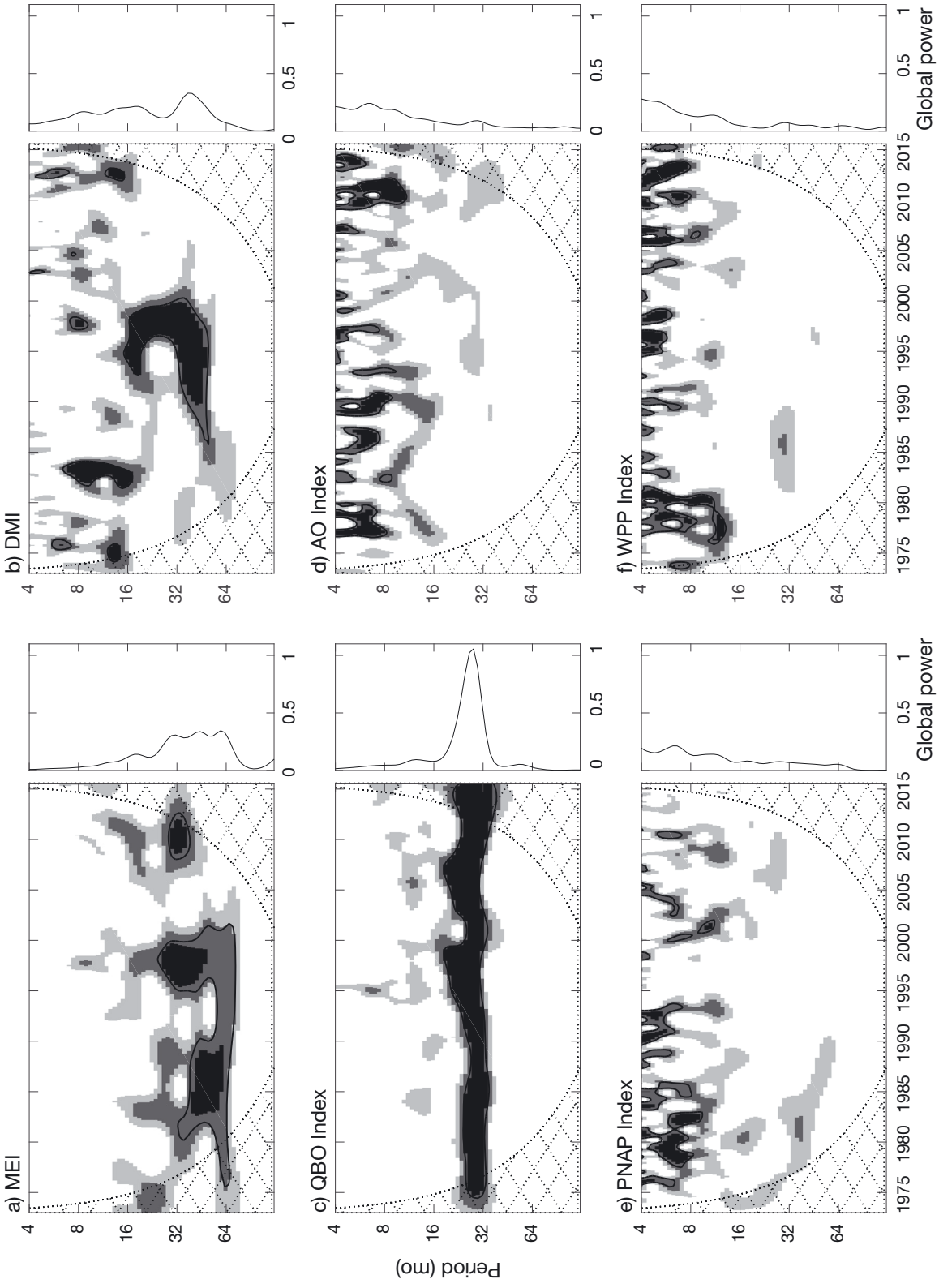

Fig. 5. Bias-rectified continuous wavelet transform (CWT) (left panels) and global power (right panels; *y*-axis also 'Period (mo)') spectra for 6 climate oscillation indices (see Fig. 4 legend for key to abbreviations) based on lag-1 autocorrelation of 0.7. Global power indicates the average power outside of the cone of influence (COI). Powers exceeding the 95% confidence level are enclosed in thick contours. Hatched areas indicate the COI

between temperature and climate oscillation at different time intervals, as discussed at the end of this section.

Of all the WTC spectra in Fig. 4, only the spectrum for MEI (Fig. 4a) reveal that the temperature covaries insignificantly with ENSO. The spectrum for MEI consists of several small very high coherence areas accompanied by random phase differences at the 4–8 mo period. This implies no connection between temperature variability and ENSO at the intraseasonal timescale, which is expected because ENSO does not exhibit significant intraseasonal variability, as seen from the CWT spectrum for MEI in Fig. 5a. At the interannual timescale, shaded areas are present in 1980–1985, 1987–1997 and 2007–2013, but the phase differences for these years vary drastically from 0° to 180°. Hence, the lack of phase-locking accompanying high coherence between the temperature and climate oscillation index for these spectra indicates an insignificant covarying relationship between ENSO with temperature.

In contrast, the WTC spectra for DMI, QBO, AO, PNAP and WPP illustrate that the temperature covaries significantly with these climate oscillation indices at certain time intervals. For the spectrum for DMI (Fig. 4b) at the 4–12 mo period, shaded areas of very high coherence are mainly present in 3 time intervals of 1977–1982, 1987–1993 and 2010–2014, where phase differences are consistently in the 315°–0° range. This suggests an in-phase relationship between IOD and temperature variability at the 4–12 mo period for these 3 intervals. In addition, the 1977–1982 interval coincides with the duration of strongest intraseasonal temperature variability (1976–1985) identified earlier. At the interannual timescale, phase differences over shaded areas at the 12–16 mo period are random, indicating that IOD does not covary with temperature at the 12–16 mo period. At the 32–64 mo period, shaded areas of very high coherence with phase differences of ~0° are found in 1985–2000. Also, the 1985–2000 duration coincides with the peak variability of IOD at the 32–64 mo period. This means that the IOD is strongly linked to interannual temperature variability in the 32–64 mo period in certain years, especially in 1985–2000. Moreover, the 1985–2000 interval matches one of the 3 durations of peak interannual temperature variability (1990–1998) identified earlier. It clarifies the relationship that IOD has with the interannual temperature variability during the 1990s. For the QBO spectrum (Fig. 4c), small areas of high coherence can be observed at the intraseasonal to shorter interannual timescales (4–28 mo), but they can be ignored as the variability of QBO is weak in this frequency band. However, at the 28–32 mo period, coinciding with the peak variability frequency band of QBO, an elongated shaded area in the 1980–2005 interval with consistent phase differences in the 45–90° range is observed. Regarding the spectrum for AO (Fig. 4d), at longer intraseasonal (>8 mo) and interannual timescales (12–32 mo), large shaded areas are present during 1975–2010. The 1975–2010 interval coincides with 2 of 3 durations of peak interannual temperature variability (1990–1998 and 2002–2010). The spectrum mainly displays an approximately in-phase connection between AO and temperature variability for these 4 durations. Regarding the spectrum for PNAP (Fig. 4e), at shorter intraseasonal timescales (4–8 mo), phase differences vary drastically from 0° to 270°, thereby indicating a lack of relationship between PNAP and temperature variability in the 4–8 mo period. However, at longer intraseasonal and interannual timescales (8–64 mo period), large shaded areas are found, particularly in 1975–2008. Their associated phase differences are in the 90–180° range, indicating that temperature variability and PNAP have a phase difference of 90–180°. The 1975–2008 interval overlaps with all of the 3 peak durations of interannual temperature variability (1980–1987, 1990–1998 and 2002–2010), which highlights the link between PNAP and interannual temperature variability at those durations. The spectrum for WPP (Fig. 4f) consists of several large patches of shaded areas throughout the entire study period at longer intraseasonal and shorter interannual timescales (4–16 mo). Besides the lone shaded area in ~2010 where its phase differences are in the 90–135° range, phase differences of other large shaded areas are consistently in the 315–0° range. Moreover, large shaded areas in 1977–1983 coincide with the time when the strongest intraseasonal temperature variability occurs (1976–1985). Similarly, very high coherence areas in 1975–1990 at the longer interannual timescale (28–64 mo), coinciding with the 1980–1990 interval of peak variability of WPP, are accompanied by consistent phase differences of ~0°. Also, by visually comparing between the WTC spectra, overall across the whole study period, the spectrum with the most extensive area of high coherence at both intraseasonal and interannual timescales belongs to that of WPP.

In addition to analysing each climate oscillation's covarying relationship with temperature, the respective contributions of various climate oscillations to temperature variability across the whole study period in general are compared. However, it is necessary to

first clarify the nature of interdependency between different climate oscillations. For example, Ashok et al. (2003) note that strong ENSO and IOD events sometimes co-occur simultaneously, and Park & Ahn (2016) found that the combined influence of AO and WPP can either diminish or reinforce the individual contributions of AO and WPP to winter temperatures over the East Asia. Indeed, the correlation matrix in Table 5 shows that some climate modes, for example ENSO and MEI, are strongly correlated with each other at the 95% confidence level. A WTC spectrum only shows the coherence between a given climate oscillation and temperature without eliminating simultaneous confounding influences of other climate oscillations. Visually comparing the coherence signals in WTC spectra of different climate oscillations alone is an unreliable method to identify which climate oscillation affects the temperature the most. Hence, a multiple linear regression analysis is conducted to resolve that issue, which measures the individual contribution of each independent variable (climate oscillation index) to the dependent variable (temperature variability). The independent variables are not significantly affected by multi-collinearity, as their variance inflation factors are <1.5, which further supports the suitability of the multiple linear regression technique in this study. Intraseasonal and interannual temperature signals are regressed on the 6 climate oscillation indices. A significant p-value at the 95% level corresponding to a climate oscillation index variable indicates a significant individual contribution of that climate mode to temperature. The regression analysis results are broadly similar among all stations, and only the results for the Tokyo station are shown in Table 6.

Comparing the results in Fig. 4 with Table 6, a significant covarying relationship between temperature and a given climate oscillation does not imply that the given climate oscillation will significantly contribute to temperature variability. As discussed earlier, the intraseasonal (interannual) temperature signals significantly covary with IOD, AO, PNAP and WPP (IOD, QBO, AO, PNAP and WPP) at certain time intervals. However, only AO, PNAP and WPP but not IOD significantly affect intraseasonal temperature variability. Also, only ENSO, QBO, AO and WPP but not PNAP significantly contribute to interannual temperature variability. In addition, although as previously discussed ENSO does not covary strongly with temperature, the regression analysis shows that ENSO contributes significantly to interannual temperature variability. There are several possible explanations for the discrepancies between the WTC and regression analysis results for ENSO, IOD and PNAP. Regarding ENSO, observational data from 1958 to 2012 show that the impacts of El Niño and La Niña on temperature over KR are asymmetric and differ across seasons (Japan Meteorological Agency 2015a,b). Temperature anomalies are only statistically significant for the El Niño but not La Niña phase, and anomalies are insignificant during the summer El Niño phase. The asymmetry and lack of continuous influence of ENSO throughout the year could explain the insignificant covarying relationship, even though a significant contribution by ENSO to interannual temperature signals is detected by the regression analysis. Focusing on IOD and PNAP, from Table 5, IOD and PNAP are strongly correlated with other climate oscillations. Thus, a possible explanation is that the significant covarying relationship between IOD and PNAP and temperature seen in the WTC spectra is due to the simultaneous confounding impacts of other climate oscillations that

Table 5. Correlation matrix between 6 climate oscillations (ENSO: El Niño–Southern Osciallation; IOD: Indian Ocean Dipole; QBO: Quasi-biennial Oscillation; AO: Arctic Oscillation; PNAP: Pacific North American Pattern; WPP: West Pacific Pattern). Following Bretherton et al. (1999), effective sample sizes

$$n_{eff} = n\left(\frac{1 - r_x r_y}{1 + r_x r_y}\right)$$

based on the lag-1 autocorrelation are used to determine significant correlations, where n is the actual sample size and r_x and r_y are lag-1 autocorrelations of 2 given time series. *Significant correlation at the 95% confidence level

	ENSO	IOD	QBO	AO	PNAP	WPP
ENSO	1	–	–	–	–	–
IOD	0.25*	1	–	–	–	–
QBO	−0.03	0.01	1	–	–	–
AO	−0.10	0.02	0.04	1	–	–
PNAP	0.18*	−0.01	−0.06	−0.28*	1	–
WPP	0.10*	0.08	+<0.01	0.09*	−0.01	1

Table 6. p-values corresponding to 6 climate oscillations (see Table 5 legend for key to abbreviations) obtained by multiple linear regression between intraseasonal and interannual temperature signals of Tokyo meteorological station with climate oscillation indices over the period January 1973–August 2015. *Significant p-value at the 95% confidence level

	ENSO	IOD	QBO	AO	PNAP	WPP
Intraseasonal	0.92	0.28	0.56	<0.01*	0.03	<0.01*
Interannual	<0.01*	0.69	0.01*	0.05*	0.22	0.05*

IOD and PNAP are strongly correlated with, and these climate oscillations do actually influence temperature variability. Another possible explanation lies in the fact that the regression analysis assesses the relationship averaged across the entire study period and should IOD and PNAP only contribute to temperature variability during certain time intervals, those contributions will be overlooked by the regression analysis. To illustrate this, using IOD as an example, since IOD only significantly covaries with interannual temperature variability in the 1980–2005 interval (from Fig. 4b), a multiple linear regression analysis is conducted using interannual temperature signals and climate mode indices in the 1980–2005 interval. Indeed, the p-value for the IOD is <0.01 over the 1980–2005 interval, suggesting that the IOD contributes significantly to interannual temperature variability in the 1980–2005 interval.

Nevertheless, the results from both WTC spectra and regression analysis are supported by other studies. Despite the fact that the WTC spectrum shows no significant covarying relationship between ENSO and temperature, the regression analysis shows that the MEI is related significantly to interannual temperature variability, which agrees with past observational data on the impact of El Niño on temperature variability (Japan Meteorological Agency 2015a,b). Also, despite the lack of a significant contribution by IOD to temperature throughout the whole study period, the WTC spectrum shows that IOD has an in-phase covarying relationship with temperature variability in KR during certain periods and years, which is consistent with Saji et al. (1999) who concluded that positive (negative) IOD indices are associated with positive (negative) temperature anomalies. The AO and temperature variability mainly exhibit an in-phase relationship in certain years and periods >8 mo, except at the ~64 mo period; moreover AO's contribution to temperature variability is significant, concurring with Park et al. (2010) who found that positive (negative) AO indices are linked to positive (negative) temperature anomalies. The WTC spectrum shows that in the 1980–2005 interval, PNAP leads temperature variability by 90–180° at the 8–16 mo period sporadically, while beyond the 28 mo period, phase differences are mainly 90°. The anti-phase relationship at the 8–16 mo period agrees with the study by Yang et al. (2002), who found that positive (negative) PNAP indices are linked to negative (positive) temperature anomalies. The lack of an anti-phase relationship at the longer interannual timescale (>28 mo), despite consistent phase differences and significant coherence, perhaps indicates that other climate oscillations well-correlated with PNAP rather than PNAP itself are contributing to the observed coherence. This is especially likely, since the regression analysis results do not show any significant contribution by PNAP to interannual temperature variability. WPP and temperature variability mainly exhibit an in-phase relationship at certain periods and years, which agrees with existing studies (e.g. Oshika et al. 2015, Park & Ahn 2016) that reveal positive (negative) WPP indices are associated with positive (negative) temperature anomalies. Finally, both the WTC spectrum and regression analysis point out the significant link between QBO and interannual temperature variability, although no existing studies have looked into their relationship.

4. CONCLUSION AND RESEARCH IMPLICATIONS

The leading modes of temperature variability, urban–rural temperature variability differences, and the influences of different climate oscillations on temperature variability are investigated for the period January 1973–August 2015 using data from 7 stations distributed across KR. It is found that the primary leading mode of temperature variability occurs at the intraseasonal timescale. Temperature variability is strongest at the intraseasonal timescale, with strongest intraseasonal (interannual) signals occurring at the 4–8 mo (~32 mo) period. The strongest temperature intraseasonal variability occurs between 1976 and 1985 with a period of 4–8 mo. Active interannual variability at the 16–64 mo period mainly occurs in 1980–1987, 1990–1998 and 2002–2010. There is no distinct difference in intraseasonal and interannual temperature variabilities between urban and rural stations. Based on the WTC spectra, the temperature of Tokyo station, which is representative of KR, is found to significantly covary with IOD, QBO, AO, PNAP and WPP but not ENSO at certain periods and years. On average over the whole study period and at the 4–120 mo period, the WPP exhibits the highest coherence with temperature amongst all climate modes. Across the whole study period on average, the multiple linear regression analysis shows that the individual contributions of AO, PNAP and WPP (MEI, QBO, AO and WPP) to intraseasonal (interannual) temperature variability are significant.

This study also shows that both intraseasonal and interannual temperature signals of climate oscillations are subject to interdecadal variations, which in turn affects the observed variations in the coherence

between a climate oscillation and temperature at different periods and years. The regression analysis results shown in this study are only applicable on average across the entire study period that spans several decades, and over the 4–12 mo and 12–120 mo periods. Since the study of individual contributions by climate modes to temperature at specific decades and frequency bands is not of interest in this paper, further research is needed to understand the individual contributions at certain decades and time intervals, perhaps with the use of partial wavelet coherence, including those periods beyond 1973. Moreover, this study only resolves the confounding influences of other climate modes within the same month when evaluating the individual contribution of a given climate mode to temperature in the regression analysis. This study did not consider the significant lag-correlation between some climate oscillations. For instance, Ashok et al. (2003) noted that the IOD and ENSO (represented by the areal averaged tropical Indian Ocean SST and Niño-3 SST index, respectively) reaches a maximum strong correlation of about 0.6 when the former lags the latter by 4 mo. Also, Horel & Wallace (1981) discovered that the summer–autumn ENSO phase can influence the winter phases of PNAP and WPP. Thus, any interest in understanding the intrinsic contribution of a given climate oscillation to temperature variability with the consideration of time-lag influences by other climate modes should be dealt with by future studies.

Acknowledgements. We express our gratitude to Drs. Chris Torrence and Liu Yonggang for assisting with the research methodology. The LULC pattern-grid maps (in shapefile format) are downloaded from http://nlftp.mlit.go.jp/ksje/index.html. The temperature data are downloaded from https://www.ncdc.noaa.gov/cdo-web/. The MEI, QBO, AO, PNAP and WPP indices are obtained from www.esrl.noaa.gov/psd/data/climateindices/list/. The DMI are extracted from www.jamstec.go.jp/frsgc/research/d1/iod/iod/dipole_mode_index.html. The CWT and WTC MATLAB packages used in this study were provided by Drs. Chris Torrence and Gilbert P. Compo as well as Dr. Aslak Grinsted, respectively. This research did not receive any specific grant from funding agencies in the public, commercial or not-for-profit sectors.

LITERATURE CITED

Addison PS (2002) The illustrated wavelet transform handbook: introductory theory and applications in science, engineering, medicine and finance. CRC Press, Boca Raton, FL

Akihiko T, Morioka Y, Behera SK (2014) Role of climate variability in the heatstroke death rates of Kanto region in Japan. Sci Rep 4:5655

Ashok K, Guan Z, Yamagata T (2003) A look at the relationship between the ENSO and the Indian Ocean Dipole. J Meteorol Soc Jpn 81:41–56

Baliunas S, Frick P, Sokoloff D, Soon W (1997) Time scales and trends in the central England temperature data (1659–1990): a wavelet analysis. Geophys Res Lett 24:1351–1354

Bretherton CS, Widmann M, Dymnikov VP, Wallace JM, Ileana B (1999) The effective number of spatial degrees of freedom of a time-varying field. J Clim 12:1990–2009

Bridgman HA, Oliver JE (2014) The global climate system: patterns, processes, and teleconnections. Cambridge University Press, Cambridge

Darby DA, Ortiz JD, Grosch CE, Lund SP (2012) 1500-year cycle in the Arctic Oscillation identified in Holocene Arctic sea-ice drift. Nat Geosci 5:897–900

Farge M (1992) Wavelet transforms and their applications to turbulence. Annu Rev Fluid Mech 24:395–458

Fujibe F (2009) Detection of urban warming in recent temperature trends in Japan. Int J Climatol 29:1811–1822

Gilman DL, Fuglister FJ, Mitchell JM Jr (1963) On the power spectrum of 'red noise'. J Atmos Sci 20:182–184

Grinsted A (2014), Cross wavelet and wavelet coherence toolbox for MATLAB. https://github.com/grinsted/wavelet-coherence (accessed on 31 Oct 2017)

Grinsted A, Moore JC, Jevrejeva S (2004) Application of the cross wavelet transform and wavelet coherence to geophysical time series. Nonlinear Process Geophys 11: 561–566

Horel JD, Wallace JM (1981) Planetary-scale atmospheric phenomena associated with the Southern Oscillation. Mon Weather Rev 109:813–829

Japan Agency for Marine–Earth Science and Technology (2003) A triangle mechanism that brings hot summer of East Asia has been revealed. https://www.jamstec.go.jp/frsgc/ eng/press/IOD/index.html

Japan Meteorological Agency (2015a) Characteristics of Japan's weather during El Niño Phase (in Japanese). www.data.jma.go.jp/gmd/cpd/data/elnino/learning/tenkou/nihon1.html

Japan Meteorological Agency (2015b) Characteristics of Japan's weather during La Niña phase (in Japanese). www.data.jma.go.jp/gmd/cpd/data/elnino/learning/tenkou/nihon2.html

Japan Meteorological Agency (2016) Relocation of Tokyo observational weather station (in Japanese). www.jma.go.jp/jma/kishou/books/sokkou/83/vol83p001.pdf

Japan Meteorological Agency (2017) Climate of Kanto/Koshin District. www.data.jma.go.jp/gmd/cpd/longfcst/en/tourist/file/Kanto_Koshin.html

Kataoka K, Matsumoto F, Ichinose T, Taniguchi M (2009) Urban warming trends in several large Asian cities over the last 100 years. Sci Total Environ 407:3112–3119

Kurita N, Fujiyoshi Y, Nakayama T, Matsumi Y, Kitagawa H (2015) East Asian monsoon controls on the inter-annual variability in precipitation isotope ratio in Japan. Clim Past 11:339–353

Liu Y, San Liang X, Weisberg RH (2007) Rectification of the bias in the wavelet power spectrum. J Atmos Ocean Technol 24:2093–2102

Lucero OA, Rodríguez NC (2000) Statistical characteristics of interdecadal fluctuations in the Southern Oscillation and the surface temperature of the equatorial Pacific. Atmos Res 54:87–104

Oke T (1982) The energetic basis of the urban heat island. QJR Meteorol Soc 108:1–24

Oke T (2006) Initial guidance to obtain representative meteorological observations at urban sites. World Meteorological Organization, Geneva

Oshika M, Tachibana Y, Nakamura T (2015) Impact of the winter North Atlantic Oscillation (NAO) on the Western Pacific (WP) pattern in the following winter through Arctic sea ice and ENSO. I. Observational evidence. Clim Dyn 45:1355–1366

Park HJ, Ahn JB (2016) Combined effect of the Arctic Oscillation and the Western Pacific Pattern on East Asia winter temperature. Clim Dyn 46:3205–3221

Park TW, Ho CH, Yang S, Jeong JH (2010) Influences of Arctic Oscillation and Madden–Julian Oscillation on cold surges and heavy snowfalls over Korea: a case study for the winter of 2009–2010. J Geophys Res D Atmospheres 115:D23122

Park TW, Ho CH, Yang S (2011) Relationship between the Arctic Oscillation and cold surges over East Asia. J Clim 24:68–83

Prokoph A, Patterson RT (2004) Application of wavelet and regression analysis in assessing temporal and geographic climate variability: Eastern Ontario, Canada as a case study. Atmos-ocean 42:201–212

Saji N, Yamagata T (2003) Possible impacts of Indian Ocean dipole mode events on global climate. Clim Res 25: 151–169

Saji NH, Goswami B, Vinayachandran P, Yamagata T (1999) A dipole mode in the tropical Indian Ocean. Nature 401: 360–363

Sakakibara Y, Owa K (2005) Urban–rural temperature differences in coastal cities: influence of rural sites. Int J Climatol 25:811–820

Santamouris M (2015) Analyzing the heat island magnitude and characteristics in one hundred Asian and Australian cities and regions. Sci Total Environ 512–513:582–598

Seo J, Choi W, Youn D, Park DSR, Kim JY (2013) Relationship between the stratospheric quasi-biennial oscillation and the spring rainfall in the western North Pacific. Geophys Res Lett 40:5949–5953

Torrence C, Compo GP (1998) A practical guide to wavelet analysis. Bull Am Meteorol Soc 79:61–78

Torrence C, Compo GP (1999) Wavelet software. http://paos.colorado.edu/research/wavelets/software.html (accessed on 31 Oct 2017)

Torrence C, Webster PJ (1999) Interdecadal changes in the ENSO–monsoon system. J Clim 12:2679–2690

Wolter K, Timlin MS (1998) Measuring the strength of ENSO events: How does 1997/98 rank? Weather 53:315–324

Yamato H, Mikami T, Takahashi H (2011) Influence of sea breeze on the daytime urban heat island in summer in the Tokyo Metropolitan Area. J Geog 120:325–340

Yang S, Lau K, Kim K (2002) Variations of the East Asian jet stream and Asian–Pacific–American winter climate anomalies. J Clim 15:306–325

Zaraket H, Saito R, Tanabe N, Taniguchi K, Suzuki H (2008) Association of early annual peak influenza activity with El Niño Southern Oscillation in Japan. Influenza Other Respir Viruses 2:127–130

Editorial responsibility: Oliver Frauenfeld, College Station, Texas, USA

Submitted: July 12, 2017; Accepted: January 3, 2018
Proofs received from author(s): April 8, 2018